Molecular determinants of Neu5Ac binding to a tripartite ATP independent periplasmic (TRAP) transporter.

Parveen Goyal[1,2,3,#,*], KanagaVijayan Dhanabalan[4], Mariafrancesca Scalise[5], Rosmarie Friemann[6], Cesare Indiveri[5,10], Renwick C.J. Dobson[7,8], Kutti R. Vinothkumar[9], and Subramanian Ramaswamy[4,*]

1. Biochemical Sciences Division, CSIR-National Chemical Laboratory, Dr Homi Bhabha Road, 411008, Pune, India.
2. Academy of Scientific and Innovative Research (AcSIR), Ghaziabad-201002, India.
3. Institute for Stem Cell Science and Regenerative Medicine, Bengaluru, Karnataka, 560065, India.[#]
4. Biological Sciences, Purdue University, West Lafayette, Indiana, 47907, USA.
5. Department DiBEST (Biologia, Ecologia, Scienze della Terra) Unit of Biochemistry and Molecular Biotechnology, University of Calabria, Via P. Bucci 4C, 87036, Arcavacata di Rende, Italy.
6. Centre for Antibiotic Resistance Research (CARe) at University of Gothenburg, Box 440, S-40530, Gothenburg, Sweden.
7. Biomolecular Interaction Centre, Maurice Wilkins Centre for Biodiscovery, MacDiarmid Institute for Advanced Materials and Nanotechnology, and School of Biological Sciences, University of Canterbury, PO Box 4800, Christchurch 8140, New Zealand.
8. Department of Biochemistry and Pharmacology, Bio21 Molecular Science and Biotechnology Institute, University of Melbourne, Parkville, Victoria, 3010, Australia
9. National Centre for Biological Sciences TIFR, GKVK Campus, Bellary Road, Bangalore-560065, India.
10. CNR, Institute of Biomembranes, Bioenergetics and Molecular Biotechnologies (IBIOM), via Amendola 122/O, 70126 Bari, Italy.

[#]Authors conducted their work for this manuscript in the associated affiliation.

* Corresponding author. E-mail: subram68@purdue.edu, parveenbmb@gmail.com

Running Title: SiaQM binding to Neu5Ac.

Keywords: Neu5Ac, TRAP transporter, *Fusobacterium nucleatum*, cryo-EM, nanobody, membrane protein.

Abbreviations: Neu5Ac, *N*-acetylneuraminic acid; TRAP, Tripartite ATP-independent periplasmic; Cryo-EM, Cryo-Electron Microscopy; DDM, n-dodecyl-β-D-maltopyranoside; SiaP, Neu5Ac TRAP substrate-binding protein; SiaQM, Neu5Ac TRAP membrane transporter.

Abstract

N-Acetylneuraminic acid (Neu5Ac) is a negatively charged nine-carbon amino-sugar that is often the peripheral sugar in human cell-surface glycoconjugates. Some bacteria scavenge, import, and metabolize Neu5Ac, or they redeploy it on their cell surfaces for immune evasion. The import of Neu5Ac by many bacteria is mediated by tripartite ATP-independent periplasmic (TRAP) transporters. We have previously reported the structures of SiaQM, a membrane-embedded component of the *Haemophilus influenzae* TRAP transport system (Currie, M J, et. al 2024). However, the published structures do not contain Neu5Ac bound to SiaQM. This information is critical for defining the mechanism of transport and for further structure-activity relationship studies. Here, we report the structure of *Fusobacterium nucleatum* SiaQM with and without Neu5Ac binding. Both structures are in an inward (cytoplasmic side) facing conformation. The Neu5Ac-bound structure reveals the interactions of Neu5Ac with the transporter and its relationship with the Na^+ binding sites. Two of the Na^+-binding sites are similar to those described previously. We discover the presence of a third metal-binding site that is further away and buried in the elevator domain. Ser300 and Ser345 interact with the C1-carboxylate group of Neu5Ac. Proteoliposome-based transport assays showed that Ser300-Neu5Ac interaction is critical for transport, whereas Ser345 is dispensable. Neu5Ac primarily interacts with residues in the elevator domain of the protein, thereby supporting the elevator with an operator mechanism. The residues interacting with Neu5Ac are conserved, providing fundamental information required to design inhibitors against this class of proteins.

Introduction

Sialic acids are nine-carbon amino sugars common on the surface of mammalian cells and on secreted molecules. *N*-Acetylneuraminic acid (Neu5Ac) and *N*-glycolylneuraminic acid (Neu5Gc) are the most prevalent forms in humans (Lewis and Lewis, 2012). A dynamic interplay between genetics, environmental cues, and cell signaling orchestrates the intricate regulation of sialic acid synthesis in mammals. These sugars frequently occupy terminal positions in glycolipids and glycoproteins and play pivotal roles in cell-cell interactions such as signaling, adhesion, and recognition (Chen and Varki, 2010). Notably, a frameshift mutation disrupts the CMP-Neu5Ac hydrolase (CMAH) gene and leads to the loss of enzymatic activity, resulting in Neu5Ac being the sole outermost sugar in humans. Conversely, primates possessing a functional CMP-Neu5Ac hydrolase, Neu5Gc is typically found as the outermost sugar (Chou et al., 1998).

This evolutionary divergence has profound consequences for the interactions between humans and pathogenic agents, including bacteria, parasites, and viruses (Varki, 2009). While commensal bacteria harness Neu5Ac as a carbon source, pathogenic bacteria, such as *Haemophilus influenzae* (*Hi*) and *Fusobacterium nucleatum* (*Fn*), evolved the ability to add Neu5Ac as the outermost sugar in their cell surface glycol-conjugates and use molecular mimicry to evade the immune system (Bell et al., 2023; Severi et al., 2007). Sialic acid is abundant in many niches [*e.g.*, [Neu5Ac] in human serum is 1.6–2.2 mM (Sillanaukee et al., 1999)]. However, the concentration of free sialic acid is often low (approximately 0.2% of the total) and much of the sialic acid is conjugated to other macromolecules on the cell surface and is, therefore, not immediately available. Secreted sialidases from bacteria cleave Neu5Ac from mucins and other biomolecules within their niche (Sillanaukee et al., 1999). Cleaved Neu5Ac is transported into the periplasm of Gram-negative bacteria via porin-like β–barrel proteins.

NanC from *E. coli* is the best-studied porin specific for sialic acids (Wirth et al., 2009).

Our laboratory has made significant strides in elucidating the structural intricacies of the proteins involved in sequestration, uptake, catabolism, and incorporation of Neu5Ac by bacteria (Bose et al., 2019; Coombes et al., 2020; Currie et al., 2021; Davies et al., 2019; Horne et al., 2020; Kumar et al., 2018; Manjunath et al., 2018; North et al., 2016; Setty et al., 2018). Bacteria rely on specialized Neu5Ac transporters within their cytosolic membranes, and four distinct classes of Neu5Ac transporters have been identified: sodium solute symporters (SSS) (North et al., 2018), major facilitator superfamily (MFS), ATP-binding cassette (ABC), and tripartite ATP-independent periplasmic (TRAP) transporters (Davies et al., 2023; Severi et al., 2021). Of particular interest are TRAP transporters that manifest as two- or three-component systems consisting of a substrate-binding protein (SiaP) and transmembrane protein (SiaQM) (Rosa et al., 2018). Deleting the sialic acid transporter (*Fn*SiaQM) abolishes Neu5Ac uptake, rendering bacteria incapable of incorporating Neu5Ac into lipopolysaccharides. Without a *Fn*SiaQM transporter, bacteria form defective biofilms, have a lower cell density, and experience higher cell death (Bozzola et al., 2022).

The first structures of SiaP were obtained from *H. influenza* in an unliganded form and bound to Neu5Ac (Johnston et al., 2008; Müller et al., 2006). The binding of Neu5Ac to SiaP results in the closure of the two domains of the protein and the mechanism has been described as a "Venus fly trap" mechanism, a common phenomenon observed in ligand-binding proteins. Structural and thermodynamic analyses of SiaP from *F. nucleatum*, *V. cholerae*, and *P. multocida* have revealed a conserved binding site, dissociation constant of Neu5Ac in the nanomolar range, and enthalpically driven substrate binding (Setty et al., 2018). Using smFRET on *Vc*SiaP, Peter and co-workers showed that conformational switching is strictly substrate-induced and that binding of the substrate stabilizes the interactions between the two

domains (Peter et al., 2021).

The second component of the TRAP transporter is the transmembrane protein SiaQM, which is characterized by two distinct domains: the Q-domain and M-domain. Two SiaQM transporter structures have been reported by cryo-EM, one from *H. influenzae* (*Hi*SiaQM) ranging from 2.95-3.70 Å resolution and another from *Protobacterium profundum* (*Pp*SiaQM) at 2.97 Å resolution (Currie et al., 2023; Davies et al., 2023; Peter et al., 2022).

The first structure of *Hi*SiaQM (3.7 Å resolution) demonstrated that it is composed of 15 transmembrane helices and two helical hairpins. *Hi*SiaQM likely functions as a monomeric unit, although a dimeric form has recently been reported (Currie et al., 2023; Peter et al., 2022). Similarly, *Pp*SiaQM has a structure with 16 transmembrane helices (Davies et al., 2023). Based on these structures, TRAP transporters are postulated to employ an elevator-type mechanism to transport substrates from the periplasm to the cytoplasm. Apart from the higher resolution dimeric HiSiaQM structure, all other structures reported were determined using the transporter complexed to a megabody complex. In both cases, the megabody was bound to the extracellular side of the QM complex, featuring a deep open cavity on the cytosolic side (**Supplementary Figure 1**). This observation suggested that the transporter was captured in an inward-facing conformation, although the higher resolution dimeric HiSiaQM structure, even without a fiducial megabody, is also in the inward-facing conformation. Notably, the transport of Neu5Ac by TRAP transporters requires at least two sodium ions (Davies et al., 2023).

In sialic acid-rich environments such as the gut and saliva, bacterial virulence often correlates with their capacity to utilize Neu5Ac as a carbon source (Almagro-Moreno and Boyd, 2010; Corfield, 2015; Haines-Menges et al., 2015). Although inhibitors targeting viral sialidases (neuraminidases) have been developed as antiviral agents (*e.g.*, oseltamivir, zanamivir, and peramivir) (Glanz et al., 2018), no drug currently targets bacterial infections by inhibiting sialic

acid sequestration, uptake, catabolism, or incorporation. Human analogs of TRAP transporters are notably absent, underscoring their potential as promising therapeutic targets for combatting bacterial infections.

Both *Hi*SiaQM and *Pp*SiaQM lack information on the Neu5Ac binding site, which was identified based on modeling studies that relied on the ligand-bound structure of *Vc*INDY (Kinz-Thompson et al., 2022). Moreover, only the structures of SiaQM in the elevator-down conformation (inward-facing) have been reported, and further conformations along the transport cycle must be elucidated. The conformation of Neu5Ac bound to the transport domain may provide clues as to how it is received from the substrate-binding protein. In this study, we present the structure of SiaQM from *F. nucleatum*, both in its unliganded form and Neu5Ac bound form. The unliganded structure has density for two Na^+-binding sites, whereas the liganded form has density for two Na^+-binding sites and one metal-binding site.

Results and Discussion

Construct design, isolation, and strategy for structural determination

The TRAP transporter from *F. nucleatum* (*Fn*SiaQM) was tagged with green fluorescent protein (GFP) at the C-terminus and expressed in BL21 (DE3) cells for protein expression and detergent stabilization trials. Detergent scouting was performed to identify the preferred detergent for *Fn*SiaQM purification using fluorescence detection size-exclusion chromatography (Kawate and Gouaux, 2006). n-Dodecyl-β-D-maltopyranoside (DDM) was chosen as it solubilized and stabilized the protein better than other detergents. *Fn*SiaQM was re-cloned into the pBAD vector with N-terminal 6X -histidine followed by Strep-tag II for large-scale purification and expressed in TOP10 (Invitrogen) cells. The reconstituted purified *Fn*SiaQM protein in DDM was eluted as a monodisperse peak in size exclusion chromatography. *Fn*SiaQM was further reconstituted in MSPD1E1 nanodiscs, along with *E. coli* polar lipids.

Initially, we attempted to determine the *Fn*SiaQM structure using X-ray crystallography. Single-particle electron cryo-microscopy (cryo-EM) was performed after failing to obtain well-diffracting crystals. To achieve a reasonable size and better particle alignment, we raised nanobodies against *Fn*SiaQM in Alpaca (Center for Molecular Medicine, University of Kentucky College of Medicine). Two high-affinity binders (T4 and T7) were identified and tested for complex formation using *Fn*SiaQM. 6X-His-tag based affinity chromatography was used to purify the nanobody from the host bacterial periplasm, producing a monodisperse peak in the size-exclusion chromatogram. Both nanobodies were added to *Fn*SiaQM and tested for complex formation. Although both nanobodies bound to the transporter, the T4 nanobody was selected over T7 because it showed higher expression. The structures of the purified *Fn*SiaQM-nanobody (T4) complexes in nanodiscs with and without Neu5Ac bound were determined

using cryo-EM.

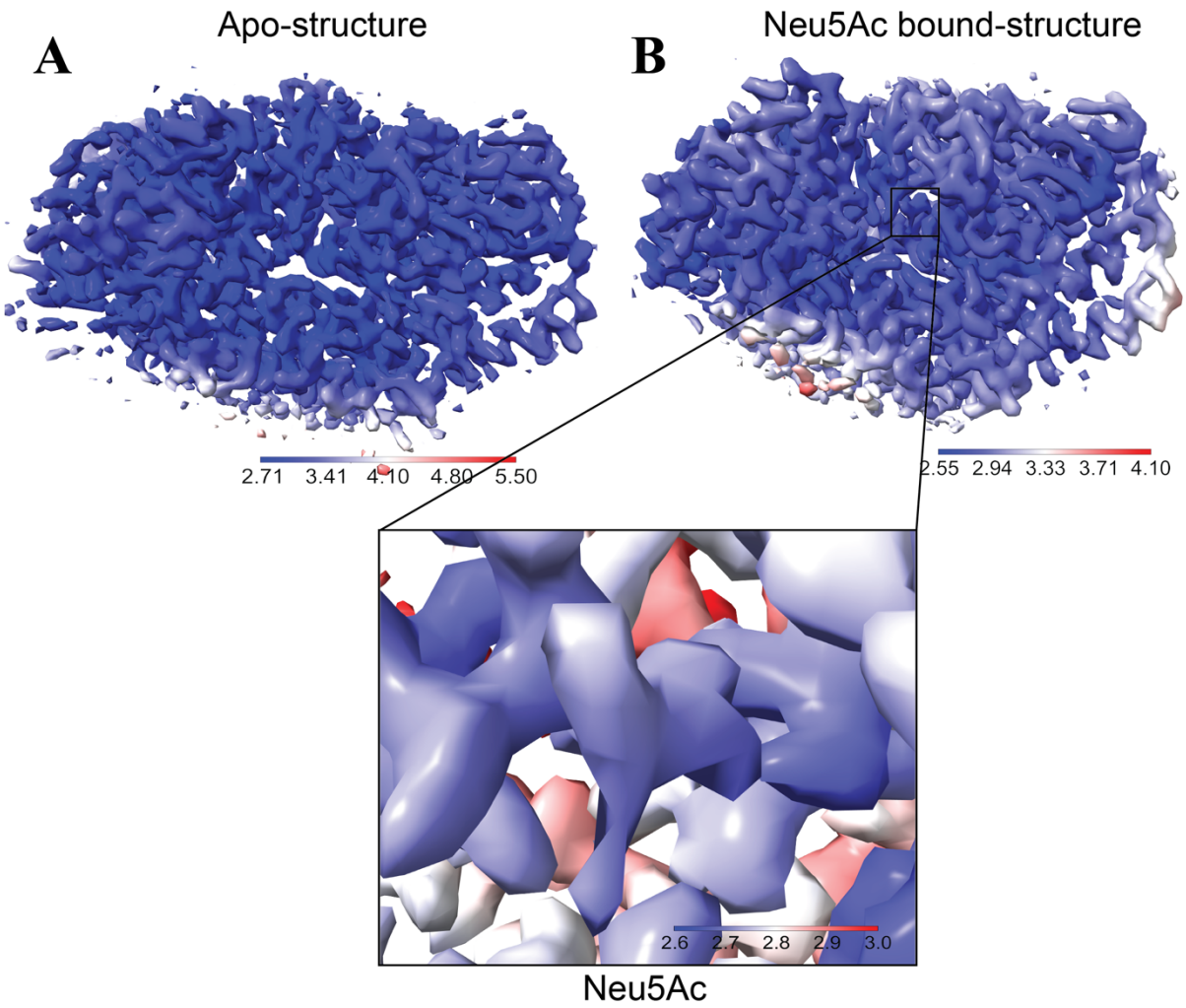

Figure 1: Local resolution maps calculated in cryoSPARC. The maps are colored from blue to red, with the higher resolution in darker blue. (A) The local resolution map of the unliganded form of the *Fn*SiaQM-nanobody complex. The interior of the *Fn*SiaQM is well-ordered. The maps are displayed at an r.m.s of 1.1. (B) The local resolution map of the Neu5Ac bound form. The insert depicts the location of Neu5Ac (center). The density for Neu5Ac is very well defined and the local resolution is about 2.6 Å.

*Structure of the Fn*SiaQM-*nanobody complex*

The nanodisc reconstituted *Fn*SiaQM, and the bound nanobody is a monomeric complex in the cryo-EM structure. The overall global resolution of the cryo-EM structure of the apo

*Fn*SiaQM-nanobody complex is ~3.2 Å. The Neu5Ac bound form had an overall resolution of ~3.16 Å. This resolution was sufficiently high to unambiguously build all helices of *Fn*SiaQM. Local resolution estimation showed that the resolution of the unliganded had a range between 2.7–5.5 Å **(Figure 1A**). The best resolution for both structures is observed in the interior of the SiaQM protein. The density of the nanodisc was visible, but of insufficient quality for model building. The local resolution range of the Neu5Ac bound is 2.55–4.1 Å (**Figure 1B**). The density of the bound Neu5Ac is clear and in the higher-resolution region (between 2.6 and 2.7 Å) (**Figure 1B, insert**). TRAP transporters, as their name suggests, comprise three units: a substrate-binding protein (SiaP) and two membrane-embedded transporter units (SiaQ and SiaM) (Severi et al., 2007). In *Fn*SiaQM, the two transporter units are fused by a long connecting helix, similar to other TRAP transporters such as *H. influenzae* TRAP (*Hi*SiaQM) (Currie et al., 2023; Peter et al., 2022). The Q-domain of *Fn*SiaQM consists of the first four long helices, which are tilted in the membrane plane. This tilting creates a large contact surface area between the Q- and M- domains, which is dominated by buried hydrophobic residues. A small connecting helix lies perpendicular to the cell membrane plane and does not contact either domain. The lack of interaction between this connecting helix and the two domains suggests that it may be redundant for transporter function. For example, *Pp*SiaQM contains two separate polypeptides and does not require a connecting helix for its function (Davies et al., 2023).

Most residues of *Fn*SiaQM and nanobody could be modeled into the cryo-EM map. The details of the structure quality and refinement parameters are shown in **Table 1** and a flow diagram for structure determination and resolution statistics is shown in **Supplementary Figure 2**. Owing to their flexibility, the N-terminal 6X histidine-tag and Strep II tags on *Fn*SiaQM were not visible in the cryo-EM maps. Similarly, the last few amino acids at the C-terminus were

not built because of poor density. While there is no direct observation, the possible mode of function of the transporter suggests that the N-terminus of *Fn*SiaQM lies on the cytoplasmic side, whereas its C-terminus lies on the periplasm side of the membrane. The nanobody is bound to the periplasmic side of *Fn*SiaQM, making no contact with the cytoplasmic side of the protein.

Superposition of the reported structures from *Hi*SiaQM and *Pp*SiaQM demonstrate that all were in inward (cytoplasmic) open and elevator-down conformations (**Supplementary Figure 1**). There are two conserved Na^+ ion binding sites in these proteins (Currie et al., 2023; Davies et al., 2023; Peter et al., 2022). The M-domain is located towards the C-terminus and comprises the bulk of the transporter. It consists of 14 transmembrane helices with two hairpins that do not cross the entire membrane.

Structurally, the M-domain can be divided into an outer variable scaffold domain and a centrally conserved transport domain. The scaffold domain is composed of transmembrane helices and serves as a support for the transport domain. It also interacts with the Q-domain to form a structurally rigid transporter domain. The Q and scaffold domains are the least conserved among the SiaQM domains, suggesting that they are not directly involved in substrate transport (**Supplementary Figure 3**).

To determine whether substrate binding resulted in conformational changes, we solved the structure of the ligand-bound form of *Fn*SiaQM. The superposition of the two structures revealed a high degree of similarity with an RMSD of 0.3 Å over all Cα atoms (**Figure 2A**). A comparison of the binding site residues revealed that they were also in a similar conformation. The transporter has a large cytoplasmic facing open cavity, suggesting that the unliganded

conformation is an inward-open conformation, while the Neu5Ac bound conformation is an inward-occluded structure. The nomenclature used for labeling the secondary structures uses a

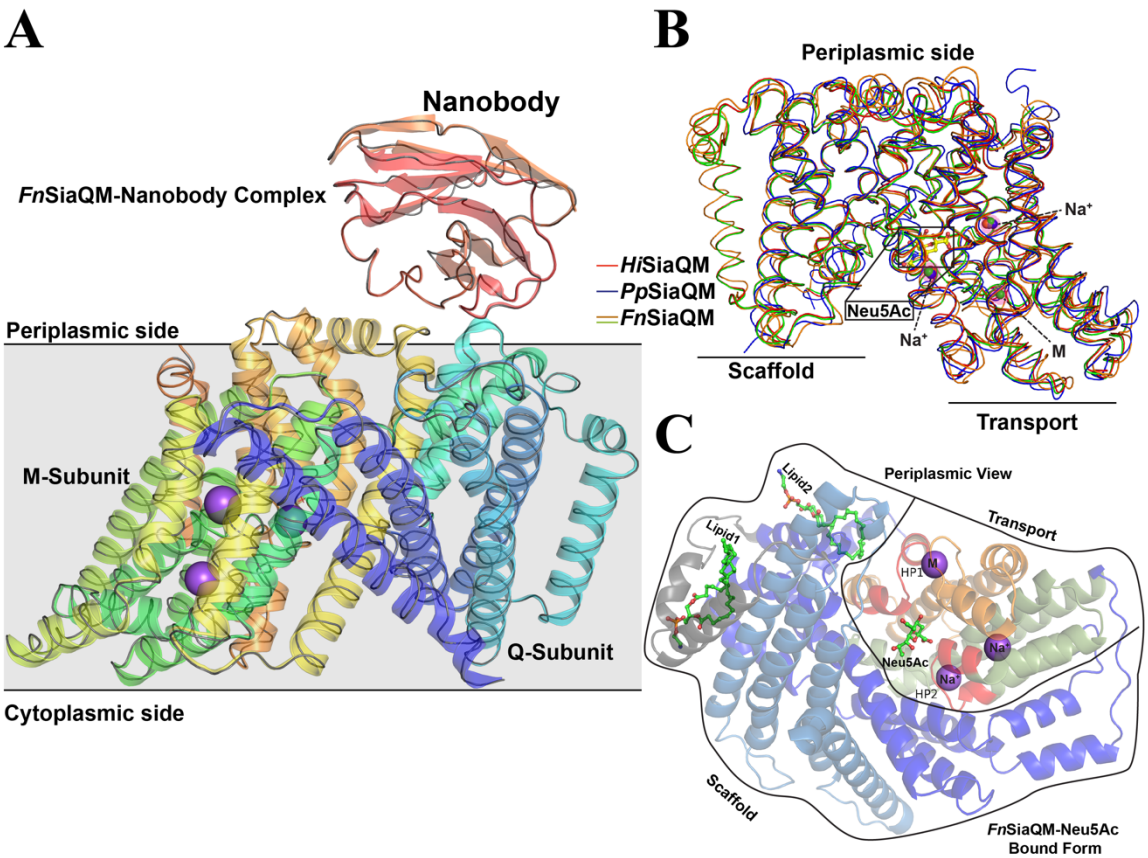

Figure 2: ***Fn*SiaQM-Nanobody complex with Neu5Ac bound form.** (A) A cartoon representation of the *Fn*SiaQM ligand bound structure. The SiaQM polypeptide has been colored in rainbow with the N-terminus starting in blue and the C-terminus ends in orange. The nanobody is shown in cartoon representation and in red color. Two of the modeled sodium sites are shown as purple spheres. A ribbon representation of the unliganded structure of *FnSiaQM* is superposed in grey. The superposition reveals that the overall structures are similar. (B) Ribbon diagram showing the superposition of the *Hi*SiaQM, *Pp*SiaQM and *Fn*SiaQM (liganded and unliganded) structures. The positions of the known Na^+ ions and metal ion (M) are inspheres, and the position of Neu5Ac is shown in ball and stick. (C) Cartoon representation of the *Fn*SiaQM structure bound to Neu5Ac. In shades of blue are the helices that form the scaffold domain. In gray is the connected domain. In olive, orange, and red is the elevator domain. HP1 and HP2, the two helix-loop-helix motifs, are in red and marked. The positions of the known Na^+ ions and metal ion (M) are in spheres, and the position of Neu5Ac is shown in ball and stick.

description of the published high-resolution *Hi*SiaQM structure (Currie et al., 2023). The elevator part of the domain has one helix-loop-helix motif called HP1 (HPin), which is directed towards the cytoplasmic side. A structurally homologous helix-loop-helix domain, HP2 (HPout), is present on the periplasmic side. Transmembrane helices have been described in detail in *Hi*SiaQM and *Pp*SiaQM structures (Davies et al., 2023; Peter et al., 2022). Interestingly, this domain has two-fold inverted symmetry, as found in other TRAP transporters. The entire domain is populated with highly conserved residues, suggesting that it may play a direct role in substrate transport (**Supplementary Figure 3**). A single molecule of Neu5Ac is bound to the aperture formed by HP1 and HP2 in the central core transport domain (**Figure 2C**). The Neu5Ac binding site has a large solvent-exposed vestibule towards the cytoplasmic side, while its periplasmic side is sealed off. In the human neutral amino acid transporter (ASCT2), which also uses the elevator mechanism, the HP1 and HP2 loops have been proposed to undergo conformational changes to enable substrate binding and release (Garaeva et al., 2019). These loops are known as gates in ASCT2. Superposition of the *Pp*SiaQM and *Hi*SiaQM structures did not result in any change in these loop structures upon substrate binding. For TRAP transporters, the substrate is delivered to the QM protein by the SiaP protein; hence, these loop changes may not play a role in ligand binding or release.

Sodium ion binding site

Transport of molecules across the membrane by TRAP transporters depends on Na^+ transport (Currie et al., 2023; Davies et al., 2023; Mulligan et al., 2009). We observed cryoEM density at conserved Na^+ binding sites and modeled two Na^+ ions in the apo- and ligand-bound forms (**Figure 3**). The two sites that are present in the unliganded form are also conserved in other reported SiaQM structures (Currie et al., 2023; Davies et al., 2023) [**Figure 2B-C**, compared with Figure 5 in (Currie et al., 2023)]. The Na1 site interacts with residues at the HP1 site and helix 5 (**Figure 3A, Supplementary Figure 4A**). The Na2 site brings together residues at the

HP2 site and a short stretch that splits helix 11 into two parts (**Figure 3A, Supplementary Figure 4B**). These two sites have been previously described (Currie et al., 2023).

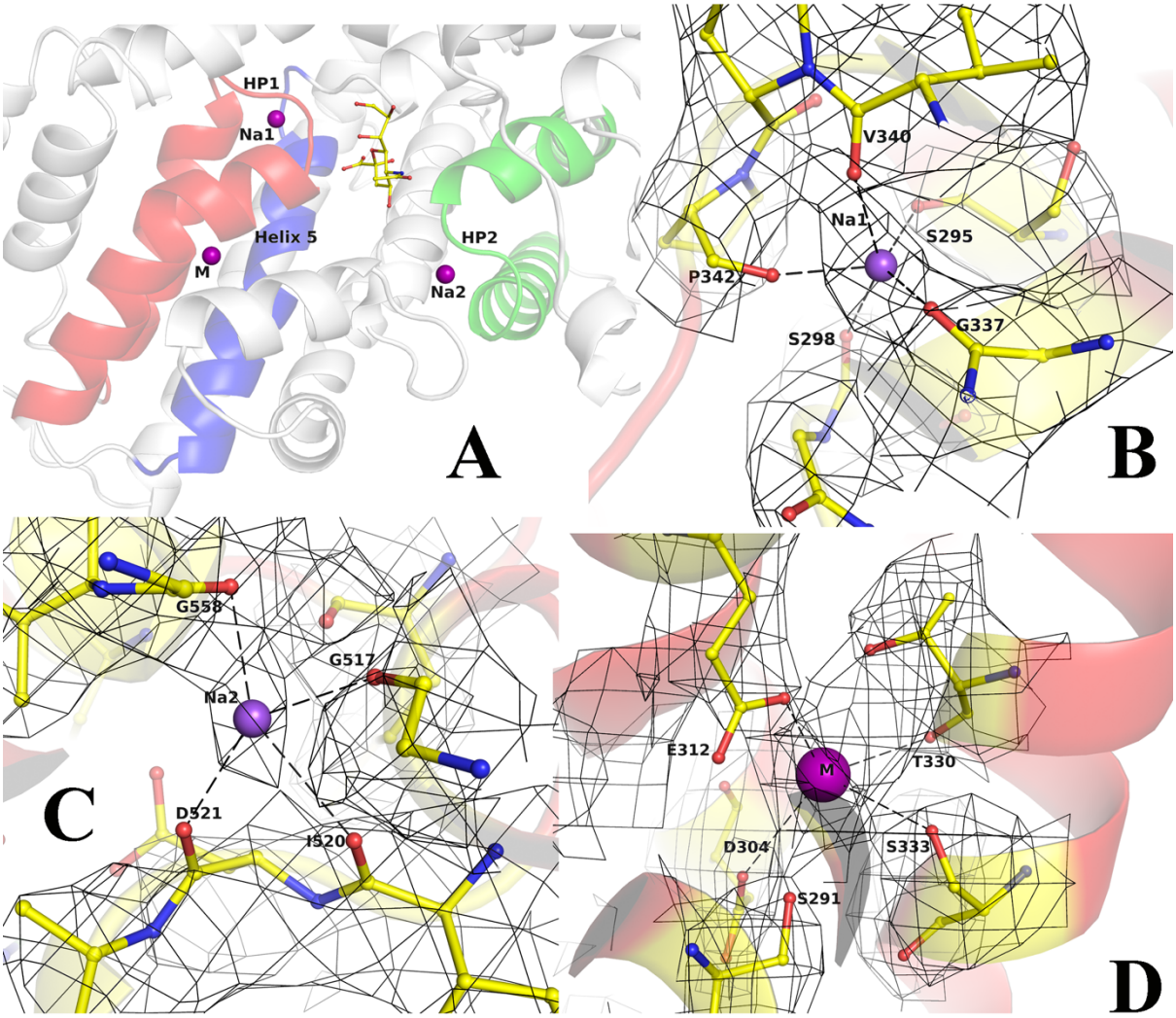

Figure 3: Binding Site of *Fn*SiaQM (A) Close-up view of the Neu5Ac and the two Na^+ and metal binding sites. In red is the HP1 helix-loop-helix. In green is the HP2 helix-loop-helix. In blue is helix 5 A, the purple spheres are the two Na^+ ion binding sites and metal binding site (M), and the bound Neu5Ac is shown in ball and stick. (B-D) Density and interaction details of the Na1, Na2, and M sites, respectively. The figures are made with a contour of 1.0 r.m.s. in PyMol.

Surprisingly, we observed density for an additional metal binding site. This site was distinctly located away from the earlier Na^+ sites and further from the Neu5Ac binding site. It interacts with helices that form HP1 and the next helix (helix 5a, **Figure 3A**). Interestingly, a similar site was observed in the SSS Neu5Ac transporter, in which the third site was located away from the others (Wahlgren et al., 2018). Peter et al. proposed that Asp304 coordinates with this Na^+ ion, showing loss-of-function when mutated to an alanine residue (Peter et al., 2022). While it is tempting to label it as a third Na^+-binding site, the metal–ligand distances are longer (**Supplementary Figure 4C**). Hence, at the current moment we conservatively designated this site as a metal-binding site. The coordinated movement of different Na^+ ions is expected to provide the energy to create conformational changes that lead to the movement of Neu5Ac from the periplasm to the cytoplasm. While we found two Na^+-binding sites and a third metal-binding site, it is not clear how the movement of these sites can cause the conformational changes required for the motion of the elevator along with the ligand. It is also unclear what the function of the third metal-binding site is beyond the mutagenesis data, which suggests that the lack of this site results in loss of function.

Lipid binding to *Fn*SiaQM

We modelled two phosphatidylethanolamine (PE) lipids in the maps of unliganded *Fn*SiaQM (**Supplementary Figure 5A and 5B**). The *Fn*SiaQM purification procedure included addition of *E. coli* polar lipids. PE is the most abundant *E. coli* polar lipid. One of the lipids binds between the connector helix and the Q-domain (**Figure 2C, Lipid1**) and is present in both the unliganded and Neu5Ac bound structure of *Fn*SiaQM. This lipid is present at a similar position in the *Hi*SiaQM structure (Currie et al., 2023). However, we found that a second lipid (**Figure 2C, Lipid2**) is bound between the stator and elevator domains only in the Neu5Ac bound structure. It is tempting to hypothesize that this lipid molecule is displaced during the

movement of the elevator domain; however, this requires further investigation.

*Activity of Fn*SiaQM

*Fn*SiaQM was reconstituted in proteoliposomes containing intraliposomal potassium, and

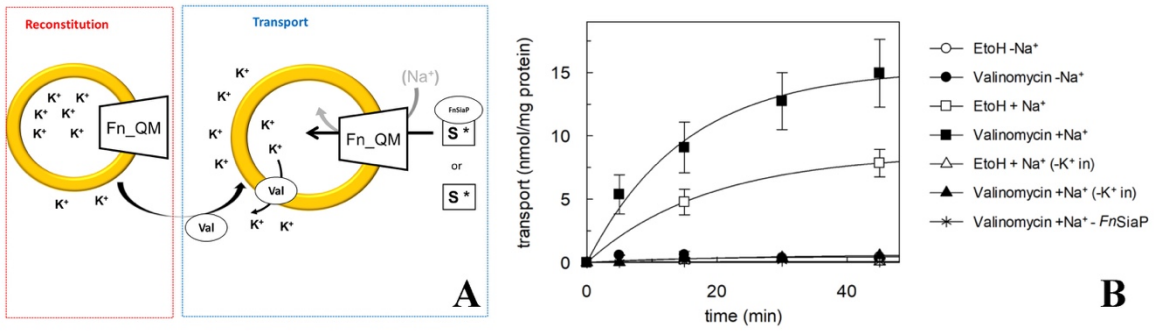

Figure 4: Proteoliposome transporter assays for *Fn*SiaQM. (A) Schematic diagram showing the experimental setup. First, *Fn*SiaQM is incorporated into proteoliposome in the presence of internal K^+. Then, valinomycin (val) is added to induce the efflux of K^+ down its concentration gradient, imposing an artificial membrane potential. To start transport measurement, *Fn*SiaP, [^{3}H]-Neu5Ac and Na^+-gluconate are added in the extraliposomal environment. (B) Time course of Neu5Ac uptake into proteoliposomes reconstituted with *Fn*SiaQM. In black circles, black squares, white triangles, black triangles, asterisks, and valinomycin, it was added to facilitate K^+ movement before transport. Ethanol was added instead of valinomycin as a control in the white circle, white square, and white triangle. In white square, black square, white triangle, black triangle, 10 mM Na^+-gluconate was added together with 5 µM [^{3}H]-Neu5Ac and 0.5 µM *Fn*SiaP; in white triangle and black triangle proteoliposomes are prepared without internal K^+; in black asterisk transport is measured in the presence of 10 mM Na^+-gluconate, 5 µM [^{3}H]-Neu5Ac and in the absence of *Fn*SiaP. Uptake data were fitted in a first-order rate equation for time course plots. Data are means ± s.d. of three independent experiments.

valinomycin was then incorporated into these proteoliposomes to establish an inner-negative membrane potential. Periplasmic binding protein (*Fn*SiaP) and radioactive Neu5Ac were added to the proteoliposomes to initiate transport (**Figure 4A**). In this experimental setup, significant accumulation of radiolabeled Neu5Ac was measured in the presence of extraliposomal Na^+-gluconate when the artificial membrane potential was imposed by the addition of valinomycin (**Figure 4B, black squares**). When ethanol was used as a control for valinomycin, a much lower accumulation of radiolabeled Neu5Ac was observed (**Figure 4B, open squares**). Importantly, transport was negligible when Na^+ was absent in the extra-liposomal environment, or when K^+ was absent in the intraliposomal environment. Transport was negligible when soluble *Fn*SiaP was omitted from the assay, further demonstrating the requirement of periplasmic binding proteins. (**Figure 4B, stars**).

Architecture of Neu5Ac binding site

While the structures of the unliganded protein and the protein bound to Neu5Ac are in the inward-open conformation, the density of the binding site of Neu5Ac is unambiguous (**Figure 5A**). The architecture of the Neu5Ac binding site is similar to that of citrate/malate/fumarate in the di/tricarboxylate transporter of *V. cholerae* (*Vc*INDY) (Kinz-Thompson et al., 2022). Neu5Ac binds to the transport domain and there are no direct interactions with the residues in the scaffold domain. The majority of the interactions are with residues in the HP1 and HP2 loops of the transport domain (**Figure 5B**). Asp521 (HP2), Ser300 (HP1), and Ser345 (helix 5) interacted with the substrate through their side chains, except for one interaction between the main chain amino group of residue 301 and the C1-carboxylate oxygen of Neu5Ac. Mutation of the residue equivalent to Asp521 has been shown to result in loss of transport (Peter et al., 2022). To evaluate the role of residues Ser-300 and Ser-345, we mutated them to

alanine and performed transport assays. The data clearly showed that the Ser300Ala mutant

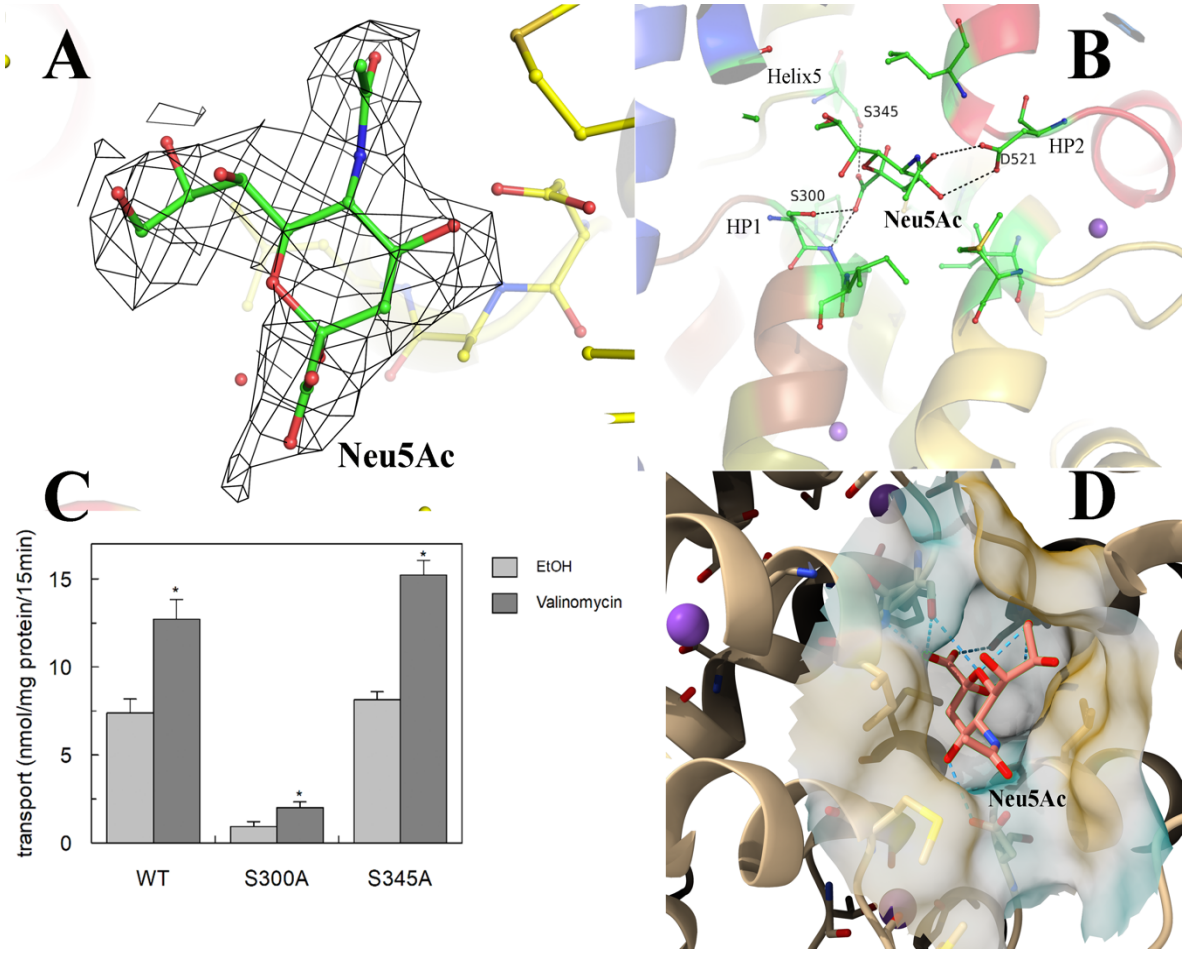

Figure 5: Validation of Neu5Ac binding pocket in *Fn*SiaQM transporter. (A) The fit of the modeled Neu5Ac into the density, contoured to 0.9 * r.m.s. (B) The interactions of Neu5Ac with side chains of interacting residues. Ser300 Oγ is 2.8 Å from the C1-carboxylate oxygen of Neu5Ac, while the main chain NH of residue 301 is 2.6 Å away. The other close polar side chain is that of Ser345γ, which is 3.3 Å away. The Neu5Ac O10 is 2.9 Å from Asp521 Oδ. (C) Transport of Neu5Ac in 15 min. Transport was started by adding 5 µM [^{3}H]-Neu5Ac, 10 mM Na^+-gluconate, and 0.5 µM *Fn*SiaP to proteoliposomes in the presence of valinomycin. Data are expressed as nmol/mg prot/15 min ± s.d. of three independent experiments]. (D) The cavity of Neu5Ac is exposed from the cytoplasmic side.

was inactive, whereas the Ser345 mutation did not affect *Fn*SiaQM functionality (**Figure 5C**). This suggests that the interaction with the residues in HP1 and HP2 is critical for transport. The

carboxylate oxygens of the C1 atom of Neu5Ac interacts with Ser300 and Ser345 and the main chain of Ala301 (**Figure 5B**). The N5 atom of the *N*-acetyl group of the sugar interacts with Asp521. These interactions are conserved even if Neu5Ac is converted into Neu5Gc, as the addition of an extra hydroxyl group at the C11 position does not break this interaction, and there is sufficient cavity space for modifications in C11 (**Figure 5D**). Cavity Plus (Wang et al.,

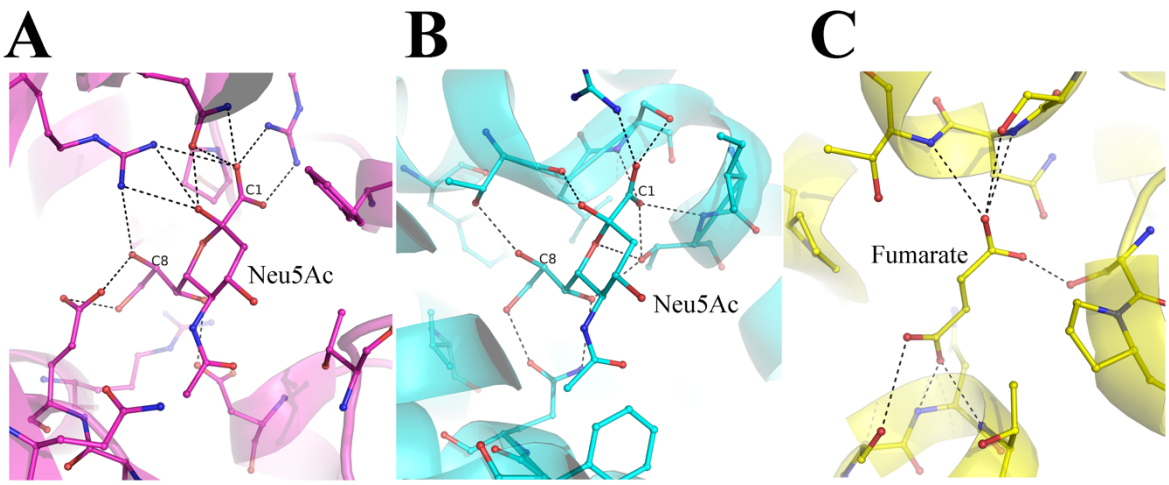

Figure 6: Comparison of Neu5Ac binding pocket (A) The interactions of Neu5Ac with the substrate binding protein SiaP from *F. nucleatum* (PDB-ID 4MNP). The C1 and the C8 carbon atoms are labeled to show the different ends of the nine-carbon sugar. (B) the interaction of Neu5Ac with the SSS-type Neu5Ac transporter (PDB-ID 5NV9). (C) The interaction of fumarate with the dicarboxylate transporter *Vc*INDY (PDB-ID 6OKZ).

2023) estimated the cavity to be 1875 $Å^3$ with a druggability score of 3631, suggesting that the environment of the binding site is highly suited for drug binding (Wang et al., 2023).

No direct measurement of K_d of Neu5Ac binding to the SiaQM region of the transporter is available. We infer from the interactions it makes and the fact that high concentrations of Neu5Ac are required to obtain a complex (30mM), the affinity may not be high. Neu5Ac binds with nanomolar affinity (K_d = 45 nM) to *Fn*SiaP (**Figure 6A**) and several electrostatic interactions stabilize this binding (Gangi Setty et al., 2014). The binding of Neu5Ac to the SSS-type transporter, which also transports Neu5Ac across the periplasmic membrane, was also stabilized by several electrostatic interactions (**Figure 6B**). The polar groups bind to both

the C1-caboxylate side of the molecule and the C8-C9 carbonyls, suggesting that SSS transporters have probably evolved to transport nine-carbon sugars such as Neu5Ac (Wahlgren et al., 2018). Interestingly, even the dicarboxylate transporter from *V. cholerae* (*Vc*INDY) binds to its ligand via electrostatic interactions with both carboxylate groups (**Figure 6C**) (Kinz-Thompson et al., 2022). The high affinity of the substrate-binding component (*Fn*SiaP) to Neu5Ac is physiologically relevant because it sequesters Neu5Ac in a volume where the concentration of Neu5Ac is very low. In contrast, because Neu5Ac is delivered to the SiaQM component by the SiaP component, the affinity could be lower, an argument also made by Peter *et. al*. in their recent work (Peter et al., 2024). The corollary of this argument is that the specificity of the transport system (or the choice of molecules that can be transported) is likely to be determined by the substrate-binding component. There is probably very little selectivity in the SiaQM component, which is also reflected by fewer interactions.

Conclusion

This is the first report of the structure of a SiaQM from the TRAP-type transporter of Gram-negative bacteria with bound Neu5Ac. The structure shows no direct interaction between Neu5Ac and Na^+ ions. The affinity of Neu5Ac for periplasmic sialic acid-binding proteins (SiaP) is in the nanomolar range, with many polar interactions (K_d=45 nM)(Gangi Setty et al., 2014). However, a few polar interactions stabilize Neu5Ac binding to the open binding pocket of SiaQM, and the affinity is probably poor. We used APBS to calculate the electrostatic charge distribution on SiaQM **(Supplementary Figure 5C)** (Jurrus et al., 2018). A view of the structure of Neu5Ac bound SiaQM from the periplasmic side towards the bound Neu5Ac shows that the sugar is bound in the cavity, the entrance of which is repulsive to the binding of a sugar that is also negatively charged. This prevents Neu5Ac from binding to the SiaQM from the cytoplasmic side. The structure of the protein in the outward-facing conformation is unknown, which will reveal how Neu5Ac is transferred from SiaP to SiaQM. While

mechanistic questions require further investigation, the precise definition of the binding pocket provided in this work is a starting point for structure-based drug discovery.

Experimental procedures

Construct design: The gene sequence encoding the TRAP transporter from *F. nucleatum* (NCBI Reference Sequence: WP_005902322.1) was synthesized and cloned into a pBAD vector using GenArt. A Strep tag was inserted in addition to the 6X-His Tag at the N-terminus to enhance the protein quality. It was cloned into pWarf (+) vector for fluorescence-detection size-exclusion chromatography (Hsieh et al., 2010).

*Protein purification of Fn*SiaQM: Expression trials and detergent scouting were performed as described by Jennifer *et al*. (Hsieh et al., 2010) For large-scale production, The *Fn*SiaQM construct in pBAD was introduced into *E. coli* strain TOP10 cells. A single colony from the transformed plate was inoculated into 150 mL of terrific broth (TB) containing 100 µg/mL ampicillin. The culture was then incubated overnight at 30 °C in a shaker incubator. The following day, 10 mL of the primary culture was transferred to a culture flask containing 1 L Terrific broth supplemented with ampicillin and incubated at 30 °C in an orbital shaker. The cultures were induced with 0.02% arabinose at an optical density (OD) of 1.5 at 600 nm and allowed to grow for an additional 18 h. Cells were harvested by centrifugation at 4000 x g for 20 min at 4 °C. The resulting cell pellet was rapidly frozen in liquid nitrogen and stored at -80 °C for future use. The cell pellet was resuspended in lysis buffer (100 mM Tris, pH 8.0, 150 mM NaCl, and 1 mM dithiothreitol (DTT)) supplemented with lysozyme, DNase, and a complete EDTA-free inhibitor cocktail (Roche). Lysis was achieved by two passes through a cell disruptor at 20 and 28 kPsi, respectively. Subsequently, cell debris and unbroken cells were pelleted by centrifugation at 10,000 x g for 30 min at 4 °C, and the supernatant was collected.

The collected supernatant was subjected to ultracentrifugation at 150,000 x g for 1 h at 4 °C to pellet the cell membranes. The membranes were then resuspended in solubilizing buffer (1% n-dodecyl-β-D-maltoside (DDM), 50 mM Tris pH 8.0, 150 mM NaCl, 10 mM imidazole, 3 mM β-ME) at a 1:10 w/v ratio and solubilized at 4 °C for two hours. The insoluble membrane components were separated by ultracentrifugation for 30 min at 100,000 × g, and the resulting supernatant was loaded onto a 5 mL His-Trap (Cytiva) column pre-equilibrated with buffer A (50 mM Tris pH 8.0, 150 mM NaCl, 10 mM imidazole, 3 mM β-ME, 0.02% DDM). The resin was extensively washed with 20 column volumes (CV) of buffer A until a stable UV absorbance was achieved in the chromatogram. The *Fn*SiaQM protein was eluted using an elution buffer (50 mM Tris, pH 8.0, 150 mM NaCl, 150 mM imidazole, 3 mM β-ME, and 0.02% DDM). The eluted fractions were pooled and used for strep-tag purification. A 5 mL Strep-Trap HP column (Cytiva) was used for subsequent purification. The column was pre-equilibrated with a buffer (100 mM Tris, pH 8.0, 150 mM NaCl, 10 mM imidazole, 3 mM β-ME, and 0.02% DDM). After loading the sample onto the column, the column was washed with 10 CV buffer (100 mM Tris pH 8.0, 150 mM NaCl, 10 mM imidazole, 3 mM β-ME, and 0.02% DDM). The *Fn*SiaQM protein was eluted in the presence of 10 mM desthiobiotin, 100 mM Tris (pH 8.0), 150 mM NaCl, 3 mM β-ME, and 0.02% DDM. The eluted fraction was concentrated using a 100 kDa Amicon filter and subsequently injected into a size-exclusion column (Superdex200 16/300 increase) in buffer (50 mM Tris pH 8.0, 150 mM NaCl, 1 mM DTT, 0.02% DDM). Size exclusion chromatography yielded a monodisperse peak for *Fn*SiaQM protein.

*Generation, isolation and purification of Fn*SiaQM-*specific nanobodies:* Generating the nanobodies was performed by the University of Kentucky Protein Core, following previously established protocols (Chow et al., 2019). Alpacas were subcutaneously injected with 100 µg

of recombinant *Fn*SiaQM in DDM once a weekly for six weeks. Peripheral blood lymphocytes were isolated from alpaca blood and used to construct a bacteriophage display cDNA library. Two rounds of phage display against the recombinant *Fn*SiaQM identified two potentially VHH-positive clones. Positive clones were confirmed by sequencing and were analyzed for nanobody components. These two nanobodies were cloned into the pMES4 vector and *E. coli* strain BL21 (DE3) was used for their expression. A single colony was inoculated into 100 mL LB medium and cultured overnight. These overnight cultures were diluted in 1 L of LB media in a 1:100 ratio. Expression was induced with 0.5 mM) when the $O.D._{600}$ reached 1.0, followed by further incubation at 28 °C for 16 h for protein production. cultures were then centrifuged at 4000 x g for 20 min at 4 °C, and periplasmic extracts were prepared using the osmotic shock method with 20% sucrose. The periplasmic extract was dialyzed to remove sucrose and filtered for affinity chromatography. This filtered fraction was loaded onto a 5 mL His-Trap (Cytiva) column pre-equilibrated with buffer B (50 mM Tris pH 8.0, 150 mM NaCl, 10 mM imidazole, and 3 mM β-ME). The column was extensively washed with 20 CV of buffer B until stable UV absorbance was observed in the chromatogram. The nanobodies were eluted using an elution buffer (50 mM Tris, pH 8.0, 150 mM NaCl, 150 mM imidazole, and 3 mM β-ME). The eluted fractions were pooled and concentrated using a 10 kDa Amicon (Sigma) filter and subsequently injected into a Superdex75 column. Both nanobodies exhibited monodisperse peaks during the size-exclusion chromatography. The peak fractions were pooled and stored at 4 °C.

*Complex formation of Fn*SiaQM-*nanobody (T4)-nanodisc (MSP1E1D1)*: MSP1E1D1 was expressed and purified following established protocols (Denisov and Sligar, 2016). The 6X-His tag was cleaved from affinity-purified MSP1E1D1 using TEV protease and the resulting product was concentrated to 5 mg/mL. For nanodisc formation, nickel affinity-eluted *Fn*SiaQM, MSP1E1D1, and *E. coli* polar lipids were combined in a molar ratio of 1:6:180 and

incubated on ice for 15 min. Nanodisc formation was initiated by adding washed Bio-Beads (200 mg dry weight per 1 mL of the protein mixture; Bio-Rad), and the mixture was rotated for two hours at 4 °C. The protein mixture was subsequently separated from the Bio-Beads using a fine needle. A two-molar excess of the T4-Nanobody was added at this step to the *Fn*SiaQM-nanodiscs. A Strep-Tag chromatography step removed the empty nanodiscs and excess T4-nanobodies. The *Fn*SiaQM-reconstituted nanodisc with the T4 nanobody were then separated from the aggregates using a Superdex200 16/300 increase size exclusion column. The fractions corresponding to the peaks were concentrated to 2.5 mg/mL and used for cryo-EM analysis. To acquire the Neu5Ac-bound structure, 30 mM Neu5Ac was incorporated into gel filtration buffer (100 mM Tris, pH 8.0, 150 mM NaCl, and 1 mM DTT).

Cryo-EM sample preparation and data collection: The *Fn*SiaQM-T4 complex at a concentration of 2.5 mg/mL was immediately applied onto UltrAuFoil R0.6/1.0 grids (300 mesh) previously subjected to glow discharge for 150 s at 25 mA. Excess fluid was removed by blotting using a Vitrobot Mark IV apparatus, and the grids were rapidly vitrified by plunging them into liquid ethane that was pre-cooled with liquid nitrogen. Subsequently, the grids were screened at a magnification of 59,000 × using a FEI Titan Krios microscope operating at 300 kV. Data were collected in counting mode at a magnification of 75,000 ×, corresponding to a pixel size of 1.07 Å using a Falcon 3 detector in counting mode.

Data processing of unliganded form: A total of 960 movies were collected for the unliganded structure. All processing was performed using the CryoSPARC software suite(Punjani et al., 2017). After patch motion correction and CTF correction, the summed images were examined and 941 micrographs were selected for particle picking. The initial particle picking (blob picker) was performed using 315 images. This was followed by 2D classification, the selection of 2D classes, and *ab initio* reconstruction into two 3D classes. One class clearly showed the

presence of the nanodisc, the protein inside, and the bound nanobody. This was refined with 49,659 particles to a resolution of 6.7 Å resolution. his 3-D map was used to create templates, template-based particle picking was performed on all 941 images, and 385,668 particles were picked. ultiple rounds of 2-D classification and selection yielded 141,272 good particles. hese particles were used for *ab initio* reconstruction in cryoSPARC(Punjani et al., 2017), followed by homogenous and nonuniform refinement. The final map resulted in an overall resolution of 3.2 Å resolution (Fourier Shell Correlation cutoff 0.143). The B-factor estimated from the Guinier plot is 125.2 $Å^2$.

Data processing of Neu5Ac-bound form: A total of 2341 images were collected. After manual inspection of the micrographs, 1752 images were selected for further processing. The template generated from the unliganded maps was used for the particle picking. After multiple rounds of 2D classification and particle pruning, 653,554 particles were used to create six *ab initio* classes. Four of these classes appeared identical and were refined to better than 4.5 Å using homogeneous refinement. After visual inspection, these four classes were combined to obtain a total of 225,006 particles. The final map was constructed using nonuniform refinement protocols in Cryo-SPARC. The map has an overall resolution of 3.17 Å at the FSC 0.143 threshold. The B-factor estimated from the Guinier plot is 135.5 $Å^2$.

Model building and model refinement: The starting model was constructed using Alphafold2 software (Evans et al., 2022). Subsequently, this model was docked within the cryo-EM map of *Fn*SiaQM unliganded form of *Fn*SiaQM. A series of iterative rounds of model building using Coot (Emsley and Cowtan, 2004) and refinement using Phenix (Adams et al., 2010) were performed to complete the model. These steps were essential for enhancing the accuracy and quality of the structural model and ensuring its congruence with experimental cryo-EM data. The refined unliganded model was used as the starting model for the substrate-bound map, and

sugars and ions were modeled. All the figures were made in UCSF Chimera or PyMOL (DeLano, 2002; Pettersen et al., 2004). The final details of the data collection, processing, and results of model building and refinement are summarized in **Table 1**.

*Reconstitution of Fn*SiaQM *into proteoliposomes:* Purified *Fn*SiaQM was reconstituted using a detergent removal method performed in batches following previously described procedures (Wahlgren et al., 2018). In summary, 50 µg *Fn*SiaQM was combined with 120 µL of 10% C12E8 detergent and 100 µL of 10% egg yolk phospholipids (w/v) in the form of sonicated liposomes. To this mixture, 50 mM K^+-gluconate and 20 mM HEPES/Tris (pH 7.0) were added to a final volume of 700 µL. The reconstitution blend was then exposed to 0.5 g of Amberlite XAD-4 resin while continuously stirred at 1200 rev/min at 23 °C for 40 min.

Transport measurements and transport assay: Following reconstitution, 600 µL of proteoliposomes were loaded onto a Sephadex G-75 column (0.7 cm diameter × 15 cm height) pre-equilibrated with 20 mM HEPES/Tris (pH 7.0) containing 100 mM sucrose to balance the internal osmolarity. Valinomycin (0.75 µg/mg phospholipid) prepared in ethanol was introduced into the eluted proteoliposomes to create a K^+ diffusion potential. Following a 10 s incubation with valinomycin, transport was initiated by adding 5 µM [^{3}H]-Neu5Ac, 0.5 µM *Fn*SiaP, and 10 mM Na^+-gluconate to 100 µL of liposomes. The initial transport rate was determined by halting the reaction after 15 min, which fell within the initial linear range of [^{3}H]-Neu5Ac uptake into the proteoliposomes, as established through time-course experiments.

The transport assay was concluded by loading each proteoliposome sample (100 µL) onto a Sephadex G-75 column (0.6 cm diameter × 8 cm height) to eliminate external radioactivity. Proteoliposomes were eluted using 1 mL of 50 mM NaCl and the collected eluate was mixed with 4 mL of scintillation mixture, followed by vortexing and counting. Data analysis was

conducted using Grafit software (version 5.0.13) using the first-order equation for time-course analysis. As specified in the figure legend, all measurements are presented as mean ± s.d. from at least three independent experiments.

Data availability

All cryo-EM data have been submitted to the EMDB (ID 38926 & 38925), and the coordinates and the model were also deposited in the Protein Data Bank (8Y4X & 8Y4W).

Supporting information

See attached supplementary figures and tables.

Acknowledgments: We would like to acknowledge the University of Kentucky's Nanobody Production Facility for its assistance. We also thank Prof. Jeff Abramson (UCLA) for providing us with the pWARF vector.

Author contributions

PG expressed and purified all the protein samples for this study. KD was involved in the production of nanobodies and protein purification. With the help of KRV, PG optimized grid preparation and data collection in cryo-EM. PG, RS, and KRV performed the computational work on the cryo-EM data. PG, KRV, and RS designed experiments. MS and CI performed the proteoliposome assays and interpreted the data. RF, RCJD, and RS conceived of the project. All the authors contributed to the writing and revision of the manuscript.

Funding and additional information

PG, KRV, and SR acknowledge the Department of Biotechnology for the cryo-EM and computing facility, funded under the B-Life grant DBT/PR12422/MED/31/287/2014. SR and RF, acknowledge funding from the Indo-Swedish collaborative grant from the DBT and the Swedish Research Council (BT/IN/Sweden/41/2013). This work was also supported by the DBT/Wellcome Trust India Alliance Fellowship (grant number IA/E/16/1/502999) awarded to PG. R.C.J.D. acknowledges the following for funding support: 1) the Marsden Fund Council from Government funding, managed by Royal Society Te Apārangi (contracts UOC1506 and

UOC2211); 2) a Ministry of Business, Innovation, and Employment Smart Ideas grant (contract UOCX1706); and 3) the Biomolecular Interactions Center (UC).

Conflict of interest

The authors have no conflicts of interest.

Ethics Statement: No human subjects were involved in the study.

References

Adams PD, Afonine PV, Bunkoczi G, Chen VB, Davis IW, Echols N, Headd JJ, Hung L-W, Kapral GJ, Grosse-Kunstleve RW, McCoy AJ, Moriarty NW, Oeffner R, Read RJ, Richardson DC, Richardson JS, Terwilliger TC, Zwart PH. 2010. PHENIX: a comprehensive Python-based system for macromolecular structure solution. *Acta Crystallographica Section D*.

Almagro-Moreno S, Boyd EF. 2010. Bacterial catabolism of nonulosonic (sialic) acid and fitness in the gut. *Gut Microbes* **1**:45–50. doi:10.4161/gmic.1.1.10386

Bell A, Severi E, Owen CD, Latousakis D, Juge N. 2023. Biochemical and structural basis of sialic acid utilization by gut microbes. *Journal of Biological Chemistry* **299**:102989. doi:10.1016/j.jbc.2023.102989

Bose S, Purkait D, Joseph D, Nayak V, Subramanian R. 2019. Structural and functional characterization of CMP-N-acetylneuraminate synthetase from *Vibrio cholerae*. *Acta Crystallographica Section D: Structural Biology* **75**:564–577. doi:10.1107/S2059798319006831

Bozzola T, Scalise M, Larsson CU, Newton-Vesty MC, Rovegno C, Mitra A, Cramer J, Wahlgren WY, Radhakrishnan Santhakumari P, Johnsson RE, Schwardt O, Ernst B, Friemann R, Dobson RCJ, Indiveri C, Schelin J, Nilsson UJ, Ellervik U. 2022. Sialic Acid Derivatives Inhibit SiaT Transporters and Delay Bacterial Growth. *ACS Chem Biol* **17**:1890–1900. doi:10.1021/acschembio.2c00321

Chen X, Varki A. 2010. Advances in the biology and chemistry of sialic acids. *ACS chemical biology* **5**:163–176.

Chou HH, Takematsu H, Diaz S, Iber J, Nickerson E, Wright KL, Muchmore EA, Nelson DL, Warren ST, Varki A. 1998. A mutation in human CMP-sialic acid hydroxylase occurred after the Homo-Pan divergence. *Proceedings of the National Academy of Sciences of the United States of America* **95**:11751–11756. doi:10.1073/pnas.95.20.11751

Chow KM, Whiteheart SW, Smiley JR, Sharma S, Boaz K, Coleman MJ, Maynard A, Hersh LB, Vander Kooi CW. 2019. Immunization of alpacas (Lama pacos) with protein antigens and production of antigen-specific single domain antibodies. *JoVE (Journal of Visualized Experiments)* e58471.

Coombes D, Davies JS, Newton-Vesty MC, Horne CR, Setty TG, Subramanian R, Moir JWB, Rosmarie Friemann X, Panjikar S, Griffin MDW, North RA, Dobson RCJ. 2020. The basis for non-canonical ROK family function in the N-acetylmannosamine kinase from the pathogen *Staphylococcus aureus*. *Journal of Biological Chemistry* **295**:3301–3315. doi:10.1074/jbc.RA119.010526

Corfield AP. 2015. Mucins: A biologically relevant glycan barrier in mucosal protection. *Biochimica et Biophysica Acta (BBA) - General Subjects* **1850**:236–252. doi:10.1016/j.bbagen.2014.05.003

Currie MJ, Davies JS, Scalise M, Gulati A, Wright JD, Newton-Vesty MC, Abeysekera GS, Subramanian R, Wahlgren WY, Friemann R, Allison JR, Mace PD, Griffin MDW, Demeler B, Wakatsuki S, Drew D, Indiveri C, Dobson RCJ, North RA. 2023. Structural and biophysical analysis of a *Haemophilus influenzae* tripartite ATP-independent periplasmic (TRAP) transporter. *eLife* **12**. doi:10.7554/eLife.92307

Currie MJ, Manjunath L, Horne CR, Rendle PM, Subramanian R, Friemann R, Fairbanks AJ, Muscroft-Taylor AC, North RA, Dobson RCJ. 2021. N-acetylmannosamine-6-phosphate 2-epimerase uses a novel substrate-assisted mechanism to catalyze amino sugar epimerization. *Journal of Biological Chemistry* **297**. doi:10.1016/j.jbc.2021.101113

Davies JS, Coombes D, Horne CR, Pearce FG, Friemann R, North RA, Dobson RC. 2019. Functional and solution structure studies of amino sugar deacetylase and deaminase enzymes from *Staphylococcus aureus*. *FEBS letters* **593**:52–66.

Davies JS, Currie MJ, North RA, Scalise M, Wright JD, Copping JM, Remus DM, Gulati A, Morado DR, Jamieson SA, Newton-Vesty MC, Abeysekera GS, Ramaswamy S, Friemann R, Wakatsuki S, Allison JR, Indiveri C, Drew D, Mace PD, Dobson RCJ. 2023. Structure and mechanism of a tripartite ATP-independent periplasmic TRAP transporter. *Nat Commun* **14**:1120. doi:10.1038/s41467-023-36590-1

DeLano WL. 2002. The PyMOL molecular graphics system. *http://www pymol org/*.

Denisov IG, Sligar SG. 2016. Nanodiscs for structural and functional studies of membrane proteins. *Nat Struct Mol Biol* **23**:481–486. doi:10.1038/nsmb.3195

Emsley P, Cowtan K. 2004. Coot: model-building tools for molecular graphics. *Acta crystallographica section D: biological crystallography* **60**:2126–2132.

Evans R, O'Neill M, Pritzel A, Antropova N, Senior A, Green T, Žídek A, Bates R, Blackwell S, Yim J, Ronneberger O, Bodenstein S, Zielinski M, Bridgland A, Potapenko A, Cowie A, Tunyasuvunakool K, Jain R, Clancy E, Kohli P, Jumper J, Hassabis D. 2022. Protein complex prediction with AlphaFold-Multimer. doi:10.1101/2021.10.04.463034

Gangi Setty T, Cho C, Govindappa S, Apicella MA, Ramaswamy S. 2014. Bacterial periplasmic sialic acid-binding proteins exhibit a conserved binding site. *Acta Cryst D* **70**:1801–1811. doi:10.1107/S139900471400830X

Garaeva AA, Guskov A, Slotboom DJ, Paulino C. 2019. A one-gate elevator mechanism for the human neutral amino acid transporter ASCT2. *Nat Commun* **10**:3427. doi:10.1038/s41467-019-11363-x

Glanz VY, Myasoedova VA, Grechko AV, Orekhov AN. 2018. Inhibition of sialidase activity as a therapeutic approach. *Drug Des Devel Ther* **12**:3431–3437. doi:10.2147/DDDT.S176220

Haines-Menges BL, Whitaker WB, Lubin JB, Boyd EF. 2015. Host Sialic Acids: A Delicacy for the Pathogen with Discerning Taste. *Metabolism and Bacterial Pathogenesis* **3**:321–342. doi:10.1128/microbiolspec.MBP-0005-2014

Horne CR, Kind L, Davies JS, Dobson RC. 2020. On the structure and function of Escherichia coli YjhC: an oxidoreductase involved in bacterial sialic acid metabolism. *Proteins: Structure, Function, and Bioinformatics* **88**:654–668.

Hsieh JM, Besserer GM, Madej MG, Bui H-Q, Kwon S, Abramson J. 2010. Bridging the gap: a GFP-based strategy for overexpression and purification of membrane proteins with intra and extracellular C-termini. *Protein Science* **19**:868–880.

Johnston JW, Coussens NP, Allen S, Houtman JCD, Turner KH, Zaleski A, Ramaswamy S, Gibson BW, Apicella MA. 2008. Characterization of the N-Acetyl-5-neuraminic Acid-binding Site of the Extracytoplasmic Solute Receptor (SiaP) of Nontypeable *Haemophilus influenzae* Strain 2019 *. *Journal of Biological Chemistry* **283**:855–865. doi:10.1074/jbc.M706603200

Jurrus E, Engel D, Star K, Monson K, Brandi J, Felberg LE, Brookes DH, Wilson L, Chen J, Liles K, Chun M, Li P, Gohara DW, Dolinsky T, Konecny R, Koes DR, Nielsen JE, Head-Gordon T, Geng W, Krasny R, Wei G-W, Holst MJ, McCammon JA, Baker NA. 2018. Improvements to the APBS biomolecular solvation software suite. *Protein Science* **27**:112–128. doi:10.1002/pro.3280

Kawate T, Gouaux E. 2006. Fluorescence-detection size-exclusion chromatography for precrystallization screening of integral membrane proteins. *Structure (London, England : 1993)* **14**:673–81. doi:10.1016/j.str.2006.01.013

Kinz-Thompson CD, Lopez-Redondo ML, Mulligan C, Sauer DB, Marden JJ, Song J, Tajkhorshid E, Hunt JF, Stokes DL, Mindell JA, Wang DN, Gonzalez RL. 2022.

Elevator mechanism dynamics in a sodium-coupled dicarboxylate transporter. doi:10.1101/2022.05.01.490196

Kumar JP, Rao H, Nayak V, Ramaswamy S. 2018. Crystal structures and kinetics of N-acetylneuraminate lyase from *Fusobacterium nucleatum*. *Acta Crystallographica Section F: Structural Biology Communications* **74**:725–732. doi:10.1107/S2053230X18012992

Lewis AL, Lewis WG. 2012. Host sialoglycans and bacterial sialidases: a mucosal perspective. *Cellular Microbiology* **14**:1174–1182. doi:10.1111/j.1462-5822.2012.01807.x

Manjunath L, Guntupalli SR, Currie MJ, North RA, Dobson RCJ, Nayak V, Subramanian R. 2018. Crystal structures and kinetic analyses of *N* -acetylmannosamine-6-phosphate 2-epimerases from *Fusobacterium nucleatum* and *Vibrio cholerae*. *Acta Crystallographica Section F Structural Biology Communications* **74**:431–440. doi:10.1107/S2053230X18008543

Müller A, Severi E, Mulligan C, Watts AG, Kelly DJ, Wilson KS, Wilkinson AJ, Thomas GH. 2006. Conservation of Structure and Mechanism in Primary and Secondary Transporters Exemplified by SiaP, a Sialic Acid Binding Virulence Factor from *Haemophilus influenzae**. *Journal of Biological Chemistry* **281**:22212–22222. doi:10.1074/jbc.M603463200

Mulligan C, Geertsma ER, Severi E, Kelly DJ, Poolman B, Thomas GH. 2009. The substrate-binding protein imposes directionality on an electrochemical sodium gradient-driven TRAP transporter. *Proceedings of the National Academy of Sciences of the United States of America* **106**:1778–83. doi:10.1073/pnas.0809979106

North RA, Wahlgren WY, Remus DM, Scalise M, Kessans SA, Dunevall E, Claesson E, Soares da Costa TP, Perugini MA, Ramaswamy S, Allison JR, Indiveri C, Friemann R, Dobson RCJ. 2018. The Sodium Sialic Acid Symporter From *Staphylococcus aureus* Has Altered Substrate Specificity. *Frontiers in Chemistry* **6**:233. doi:10.3389/fchem.2018.00233

North RA, Watson AJ, Pearce FG, Muscroft-Taylor AC, Friemann R, Fairbanks AJ, Dobson RC. 2016. Structure and inhibition of N-acetylneuraminate lyase from methicillin-resistant *Staphylococcus aureus*. *FEBS letters* **590**:4414–4428.

Peter MF, Gebhardt C, Glaenzer J, Schneberger N, de Boer M, Thomas GH, Cordes T, Hagelueken G. 2021. Triggering Closure of a Sialic Acid TRAP Transporter Substrate Binding Protein through Binding of Natural or Artificial Substrates. *Journal of Molecular Biology* **433**:166756. doi:10.1016/j.jmb.2020.166756

Peter MF, Ruland JA, Depping P, Schneberger N, Severi E, Moecking J, Gatterdam K, Tindall S, Durand A, Heinz V, Siebrasse JP, Koenig P-A, Geyer M, Ziegler C, Kubitscheck U, Thomas GH, Hagelueken G. 2022. Structural and mechanistic analysis of a tripartite ATP-independent periplasmic TRAP transporter. *Nat Commun* **13**:4471. doi:10.1038/s41467-022-31907-y

Peter MF, Ruland JA, Kim Y, Hendricks P, Schneberger N, Siebrasse JP, Thomas GH, Kubitscheck U, Hagelueken G. 2024. Conformational coupling of the sialic acid TRAP transporter *Hi*SiaQM with its substrate binding protein *Hi*SiaP. *Nat Commun* **15**:217. doi:10.1038/s41467-023-44327-3

Pettersen EF, Goddard TD, Huang CC, Couch GS, Greenblatt DM, Meng EC, Ferrin TE. 2004. UCSF Chimera—a visualization system for exploratory research and analysis. *Journal of computational chemistry* **25**:1605–1612.

Punjani A, Rubinstein JL, Fleet DJ, Brubaker MA. 2017. cryoSPARC: algorithms for rapid unsupervised cryo-EM structure determination. *Nature Methods* **14**:290–296. doi:10.1038/nmeth.4169

Rosa LT, Bianconi ME, Thomas GH, Kelly DJ. 2018. Tripartite ATP-Independent Periplasmic (TRAP) Transporters and Tripartite Tricarboxylate Transporters (TTT): From Uptake to Pathogenicity. *Front Cell Infect Microbiol* **8**:33. doi:10.3389/fcimb.2018.00033

Setty TG, Mowers JC, Hobbs AG, Maiya SP, Syed S, Munson RS, Apicella MA, Subramanian R. 2018. Molecular characterization of the interaction of sialic acid with the periplasmic binding protein from *Haemophilus ducreyi*. *Journal of Biological Chemistry* **293**:20073–20084. doi:10.1074/jbc.RA118.005151

Severi E, Hood DW, Thomas GH. 2007. Sialic acid utilization by bacterial pathogens. *Microbiology* **153**:2817–2822. doi:10.1099/mic.0.2007/009480-0

Severi E, Rudden M, Bell A, Palmer T, Juge N, Thomas GH. 2021. Multiple evolutionary origins reflect the importance of sialic acid transporters in the colonization potential of bacterial pathogens and commensals. *Microb Genom* **7**:000614. doi:10.1099/mgen.0.000614

Sillanaukee, Pönniö, Jääskeläinen. 1999. Occurrence of sialic acids in healthy humans and different disorders. *European Journal of Clinical Investigation* **29**:413–425. doi:10.1046/j.1365-2362.1999.00485.x

Varki A. 2009. Multiple changes in sialic acid biology during human evolution. *Glycoconj J* **26**:231–245. doi:10.1007/s10719-008-9183-z

Wahlgren WY, Dunevall E, North RA, Paz A, Scalise M, Bisignano P, Bengtsson-Palme J, Goyal P, Claesson E, Caing-Carlsson R, Andersson R, Beis K, Nilsson UJ, Farewell A, Pochini L, Indiveri C, Grabe M, Dobson RCJ, Abramson J, Ramaswamy S, Friemann R. 2018. Substrate-bound outward-open structure of a Na^+-coupled sialic acid symporter reveals a new Na^+site. *Nature Communications* **9**:1753. doi:10.1038/s41467-018-04045-7

Wang S, Xie J, Pei J, Lai L. 2023. CavityPlus 2022 Update: An Integrated Platform for Comprehensive Protein Cavity Detection and Property Analyses with User-friendly Tools and Cavity Databases. *Journal of Molecular Biology*, Computation Resources for Molecular Biology **435**:168141. doi:10.1016/j.jmb.2023.168141

Wirth C, Condemine G, Boiteux C, Bernèche S, Schirmer T, Peneff CM. 2009. NanC Crystal Structure, a Model for Outer-Membrane Channels of the Acidic Sugar-Specific KdgM Porin Family. *Journal of Molecular Biology* **394**:718–731. doi:10.1016/j.jmb.2009.09.054

Supplementary Data.

Supplementary Figure 1: Superposition of SiaQM structures.

Supplementary Figure 2: Cryo-EM workflow and analysis of the *Fn*SiaQM-nanobody complex.

Supplementary Figure 3: Sequence comparison of SiaQM from *F. nucleatum*, *H. influenzae* and *P. profundum.*

Supplementary Figure 4: Detail architecture of the Na^+ and Metal binding sites.

Supplementary Figure 5: A and B Density of Lipid1 and Lipid2. C. Electrostatic charge distribution on the surface of SiaQM.

Table 1: Details of cryo-EM data collection, processing, refinement and built model.

Data collection and processing **EMDB** **PDB**	Apo form 38926 8Y4X	Neu5Ac-bound 38925 8Y4W
Magnification	75000	75000
Voltage (kV)	300	300
Electron dose (e^-/Å^3)	27.7	24.67
Defocus Range (μm)	1800-3000	1600-2800
Pixel size (Å)	1.07	1.07
Symmetry imposed	C1	C1
Initial particle images (no.)	385668	653554
Final particle images (no.)	141272	225006
Map resolution (Å)	3.20	3.16
FSC threshold	0.143	0.143
Map resolution range (Å)	2.7-5.5	2.6-4.1
Refinement		
Model composition		
Non-hydrogen atoms	5801	5873
Protein residues	732	732
Ligand	2 Na^+;1 Lipid	3 Na^+; 2 Lipid; 1 Neu5Ac
B-factor (Å^2)		
Protein (mean)	46.72	43.60
Ligand (mean)	45.88	56.25
R.m.s deviations		
Bond lengths (Å)	0.005	0.004
Bond angles (°)	0.531	0.512
Validation		
MolProbity score	1.76	1.54
Clashscore	5.57	5.07
CaBALM outliers (%)	1.52	1.52
Rotamer outliers (%)	1.77	1.13
Ramachandran plot (%) (Favored/Allowed/Disallowed)	(96.02/3.98/0)	(96.43/3.57/0)

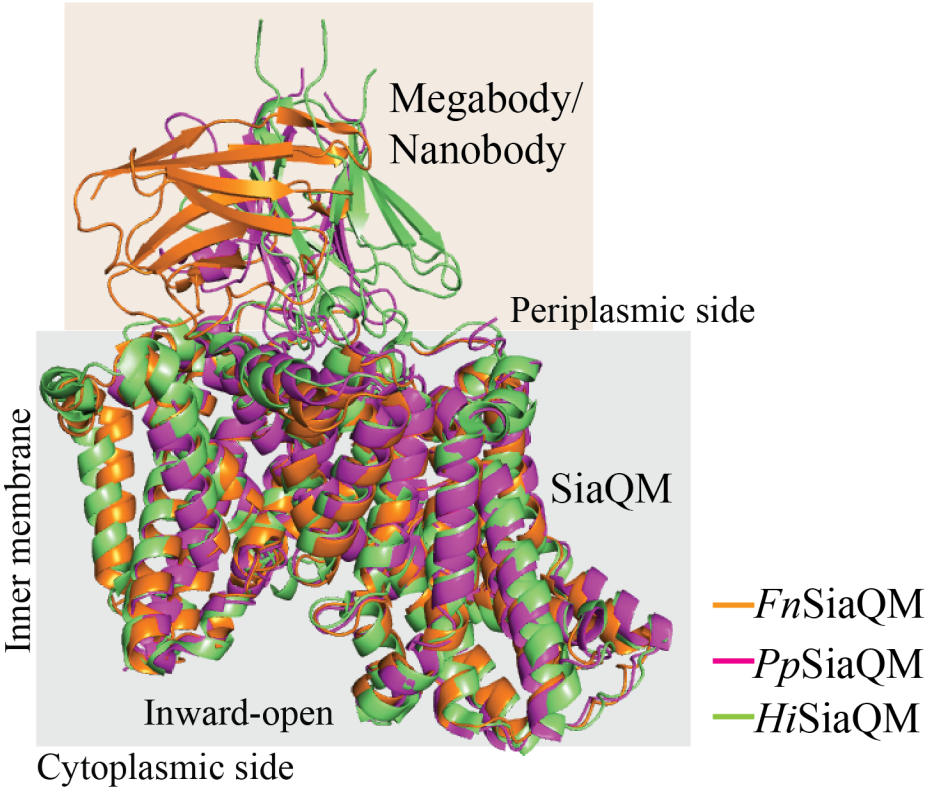

Supplementary Figure 1. Superposition of SiaQM structure from *F. nucleatum*, *H. influenzae* and *P. profundum* with respective bound nanobody or megabody. The structures were in inward-open conformation.

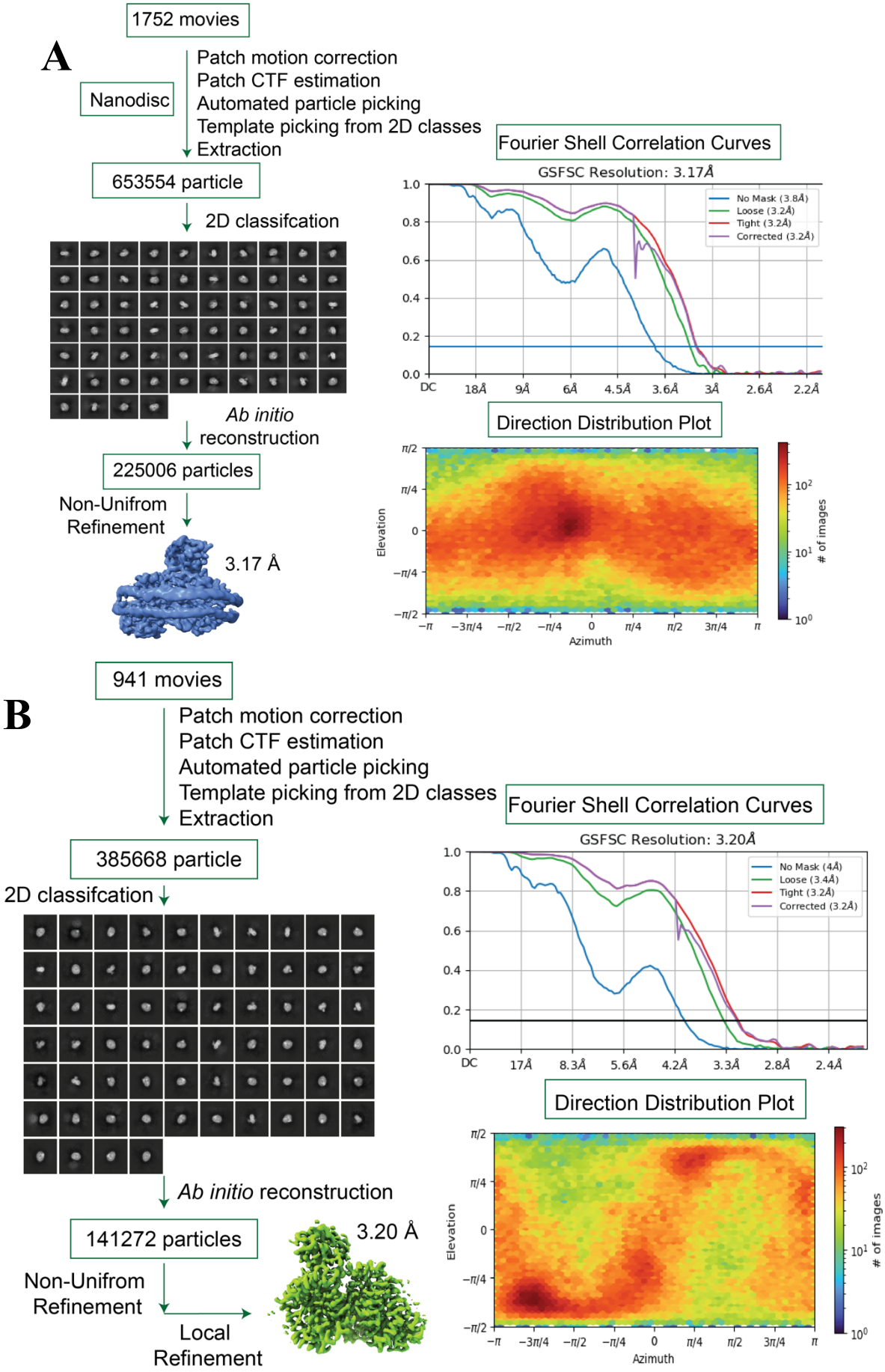
A
1752 movies
Nanodisc
Patch motion correction
Patch CTF estimation
Automated particle picking
Template picking from 2D classes
Extraction
653554 particle
2D classifcation
Ab initio reconstruction
225006 particles
Non-Unifrom Refinement
3.17 Å
Fourier Shell Correlation Curves
GSFSC Resolution: 3.17Å
No Mask (3.8Å)
Loose (3.2Å)
Tight (3.2Å)
Corrected (3.2Å)
DC
18Å
9Å
6Å
4.5Å
3.6Å
3Å
2.6Å
2.2Å
Direction Distribution Plot
Elevation
Azimuth
# of images
B
941 movies
Patch motion correction
Patch CTF estimation
Automated particle picking
Template picking from 2D classes
Extraction
385668 particle
2D classifcation
Ab initio reconstruction
141272 particles
Non-Unifrom Refinement
Local Refinement
3.20 Å
Fourier Shell Correlation Curves
GSFSC Resolution: 3.20Å
No Mask (4Å)
Loose (3.4Å)
Tight (3.2Å)
Corrected (3.2Å)
DC
17Å
8.3Å
5.6Å
4.2Å
3.3Å
2.8Å
2.4Å
Direction Distribution Plot
Elevation
Azimuth
# of images

Supplementary Figure 2. Cryo-EM workflow and analysis of the *Fn*SiaQM protein. A) and B) a detailed workflow outlining the steps involved in cryo-EM image acquisition and processing, leading to the generation of both the bound and Apo structures of the *Fn*SiaQM protein, respectively. The selected 2D class average utilized for *ab initio* reconstructions is depicted, and the optimal 3D reconstructions serve as reference models for subsequent non-uniform refinement. Masks generated using RELION 3.0 were applied, and the resulting maps underwent iterative rounds of local refinement. Fourier shell correlation (FSC) curves for the final 3D reconstructions of the bound and Apo structures of the *Fn*SiaQM protein are presented.

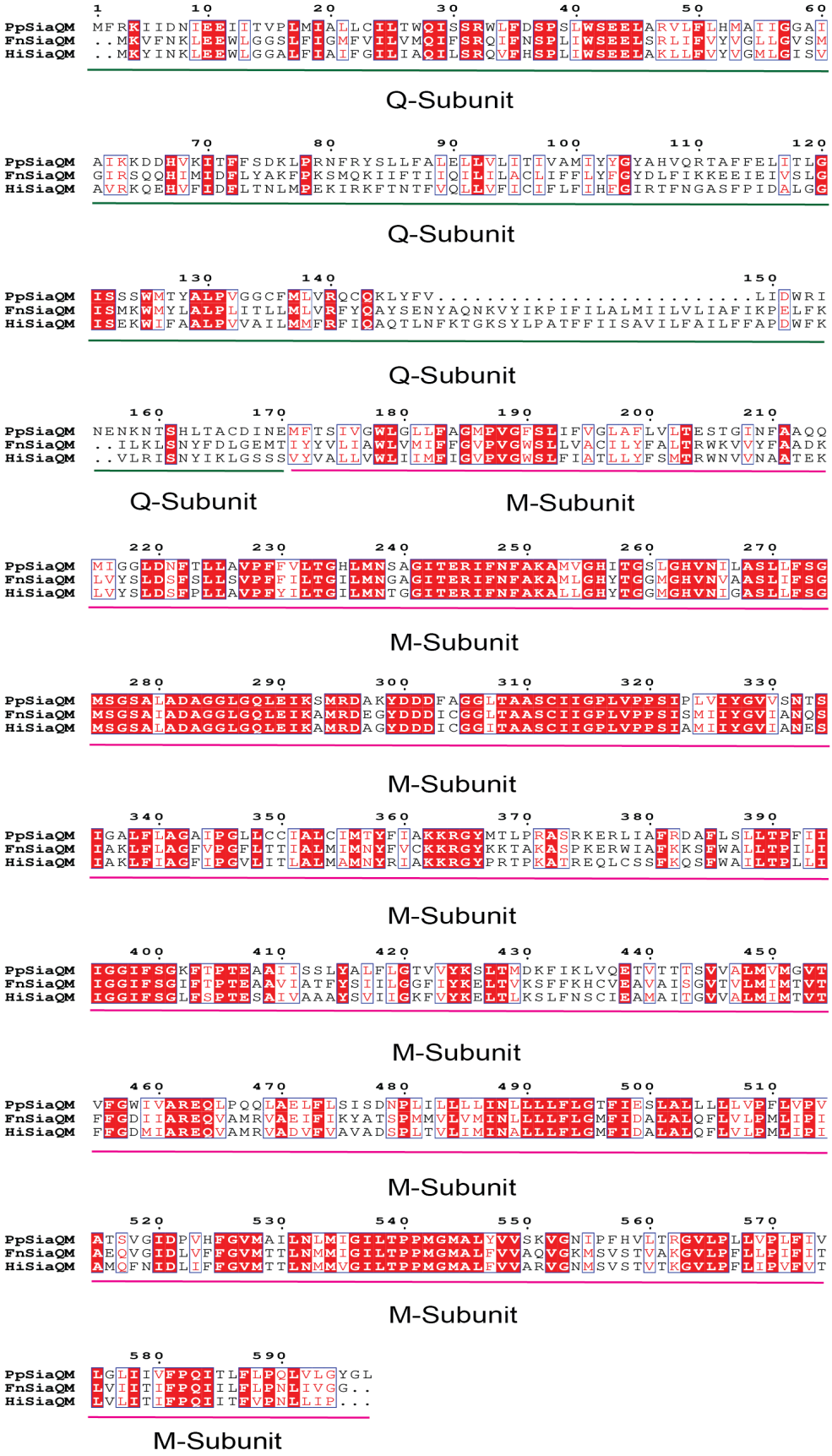

Supplementary Figure 3. SiaQM protein sequence alignment. SiaQM protein sequences from *Photobacterium profundum*, *Haemophilus influenzae,* and *Fusobacterium nucleatum*. Protein sequences were aligned using ESPript 3.

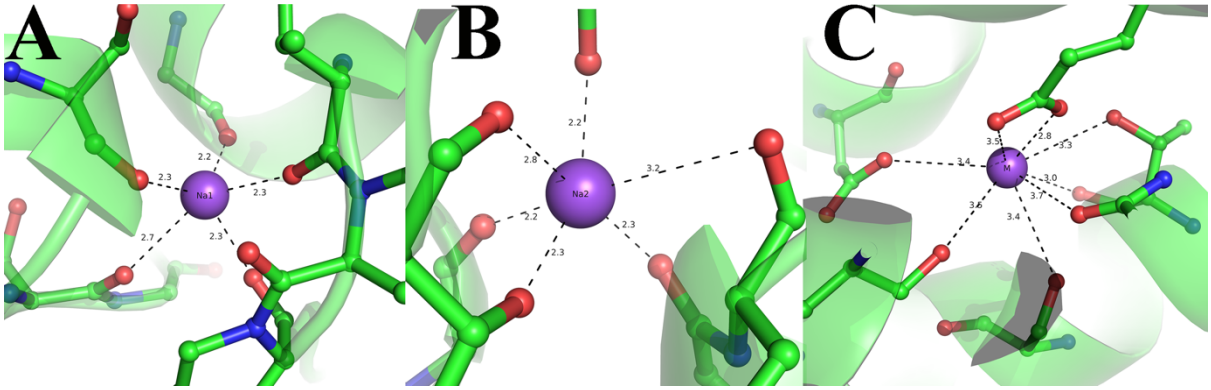

Supplementary Figure 4. A) Na1 site coordination and its interactions with neighboring amino acids; B) Na2 site coordination and its interactions with neighboring amino acids; C) Metal binding site coordination and its interactions with neighboring amino acids.

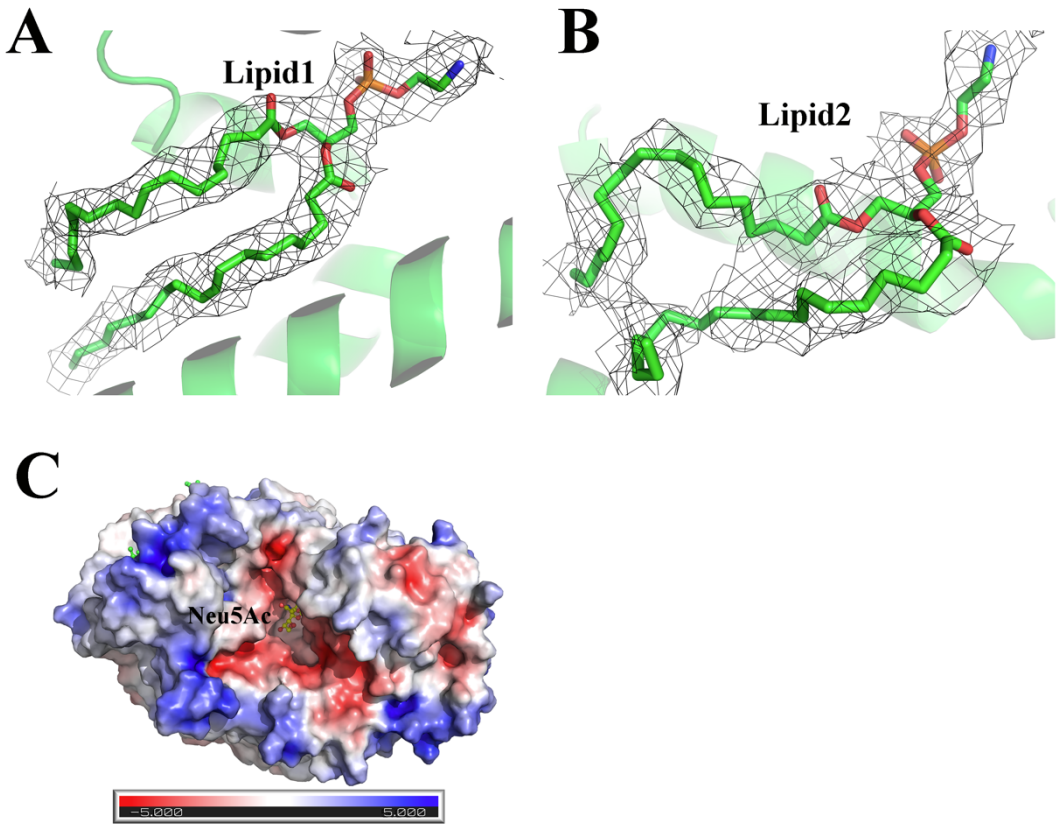

Supplementary Figure 5. A and B. Density of two lipids (Lipid1 and Lipid2) was observed in the scaffold side of *Fn*SiaQM (contour of 1.0 r.m.s. in PyMol). C. Electrostatic potential visualization of *Fn*SiaQM. Neu5Ac density in the binding pocket of *Fn*SiaQM. ABPS colored in the range from -5 to +5.